Inorganic Chemistry

Article

pubs.acs.org/IC

Charge-Density Distribution and Electrostatic Flexibility of ZIF-8 Based on High-Resolution X-ray Diffraction Data and Periodic Calculations

Sladjana B. Novaković,*[†] Goran A. Bogdanović,*[†] Christian Heering,[‡] Gamall Makhloufi,[‡] Djordje Francuski,[§] and Christoph Janiak*[‡]

[†]Vinča Institute of Nuclear Sciences, University of Belgrade, P.O. Box 522, 11001 Belgrade, Serbia

[‡]Institut für Anorganische Chemie und Strukturchemie, Heinrich-Heine-Universität Düsseldorf, Universitätsstrasse 1, 40225 Düsseldorf, Germany

[§]Institute of Molecular Genetics and Genetic Engineering, University of Belgrade, Vojvode Stepe 444a, 11010 Belgrade, Serbia

Supporting Information

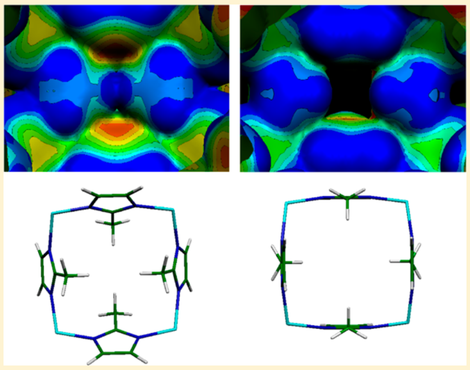

ABSTRACT: The electron-density distribution in a prototypical porous coordination polymer ZIF-8 has been obtained in an approach combining high-resolution X-ray diffraction data and Invariom refinement. In addition, the periodic quantum-chemical calculation has been used to describe the theoretical density features of ZIF-8 in the same geometry (**m1**) and also in a "high-pressure" form of ZIF-8 (**m2**) characterized by conformational change with respect to the methylimidazolate linker. A thorough comparison of the electronic and electrostatic properties in two limiting structural forms of ZIF-8 proposes additional aspects on diffusion and adsorption processes occurring within the framework. The dimensions of the four-membered (FM) and six-membered (SM) apertures of the β cage are reliably determined from the total electron-density distribution. The analysis shows that FM in **m2** becomes competitive in size to the SM aperture and should be considered for the diffusion of small molecules and cations. Bader's topological analysis (quantum theory of atoms in molecules) shows similar properties of both ZIF-8 forms. On the other hand, analysis of their electrostatic properties reveals tremendous differences. The study suggests exceptional electrostatic flexibility of the ZIF-8 framework, where small conformational changes lead to a significantly different electrostatic potential (EP) distribution, a feature that could be important for the function and dynamics of the ZIF-8 framework. The cavity surface in **m1** contains 38 distinct regions with moderately positive, negative, or neutral EP and weakly positive EP in the cavity volume. In contrast to **m1**, the **m2** form displays only two regions of different EP, with the positive one taking the whole cavity surface and the strong negative one localized entirely in the FM apertures. The EP in the cavity volume is also more positive than that in **m1**. A pronounced influence of the linker reorientation on the EP of the ZIF-8 forms is related to the high symmetry of the system and to an amplification of the electrostatic properties by cooperative effects of the proximally arranged structural fragments.

INTRODUCTION

Zeolitic imidazolate framework 8 (ZIF-8) is a prototypical metal−organic framework/porous coordination polymer (MOF/PCP) that shows great potential for several applications, in particular high-capacity storage and separation of gases, catalysis, sensing, and optics.[1−7] ZIFs have structures similar to aluminosilicates (zeolites).[8] Its robustness and comparatively facile and inexpensive synthesis make ZIF-8 an ideal material for investigations on permanently porous 3D frameworks in general.[9] The adsorptive properties of gases (especially H_2 and CO_2) in ZIF-8 and their understanding are the subject of recent publications.[10,11] ZIF-8 is composed of tetrahedrally nitrogen-coordinated Zn atoms linked by 2-methylimidazolate (MeIm) ligands (Figure 1). The infinite arrangements of these building blocks results in the formation of large cavities, estimated to be ~11.6 Å in diameter.[1,2] Figure 1c shows the structure of an individual cavity of ZIF-8, which contains eight six-membered (SM) hexagonal and six four-membered (FM) square pore apertures. Like in the mineral sodalite, in ZIF-8 each face of the cavity is shared with a neighboring one, forming an extended porous material (Figure 1d). In addition to high porosity and large surface area (Brunauer−Emmett−Teller, BET; 1630 m^2 g^{-1}), ZIF-8 exhibits remarkable thermal (550 °C) and chemical stability, attributed to the strong Zn−MeIm linkage. Because of the small size of the SM window (estimated to be ~3.4 Å in diameter),[1] ZIF-8 was initially considered appropriate for the separation of H_2 from other gases.[12] Several experimental and theoretical studies, however, showed that molecules with larger diameters (N_2,[13,14] I_2,[15] CH_4,[16] and other short hydro-

Received: November 26, 2014
Published: February 23, 2015

DOI: 10.1021/ic5028256
Inorg. Chem. 2015, 54, 2660−2670

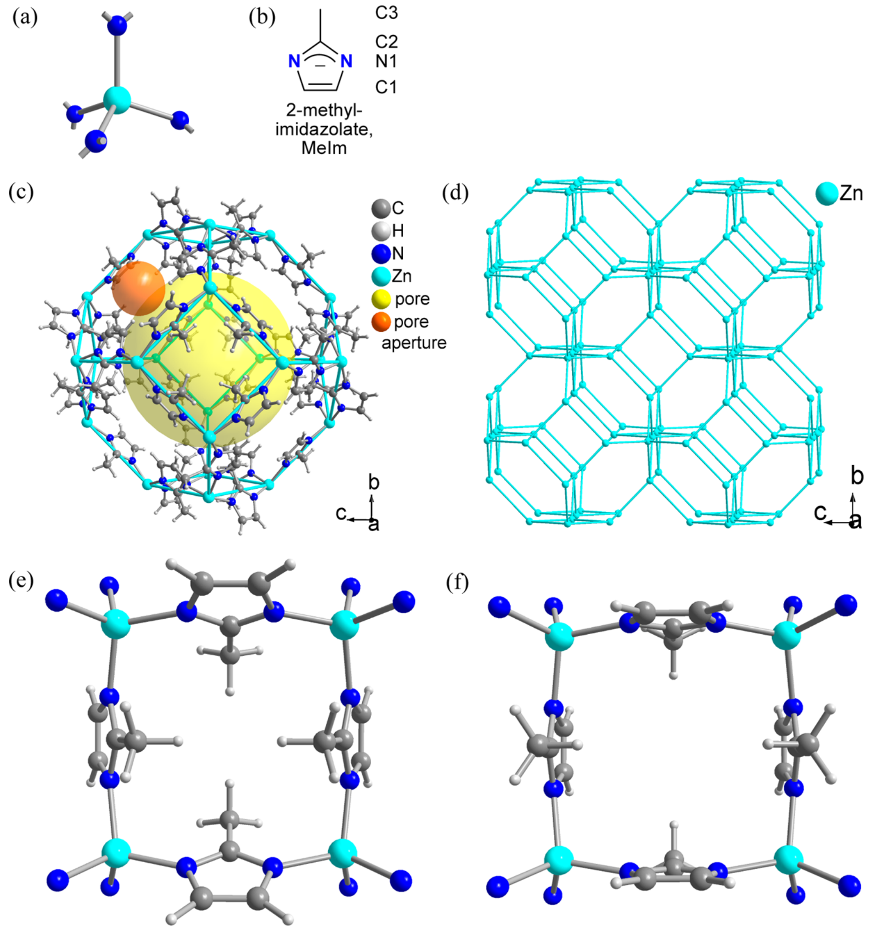

Figure 1. (a) Secondary building unit of tetrahedral, nitrogen-coordinated Zn atoms and (b) bridging ligand in ZIF-8. (c) Structure of the ZIF-8 cavity. MeIm ligands bridge between Zn atoms and span the edges of a cuboctahedral β cage in a sodalite network (d), which is depicted by light-blue topological lines between the Zn atoms. The yellow sphere with a diameter of 12 Å shows the inner pore of the sodalite cage, and the orange sphere with a diameter of 3.4 Å visualizes the pore aperture window of the SM hexagonal rings. Both spheres take into account the van der Waals radii of the framework atoms. The figure was drawn with *Diamond*[24] from a deposited CIF file (CSD-Refcode VELVOY[2]). (e and f) FM apertures from the refinement of experimental models **m1a** (e) and **m2** (f).

carbons,[17,18] CO_2,[19,20] caffeine,[21] and butanol[22]) can also diffuse into the ZIF-8 structure. Recent investigations explained that, either at a very high pressure[23] or during gas uptake,[13,14,19] ZIF-8 can undergo structural changes by reorientation of the MeIm linker, which can lead to an enlargement of the cavity windows. These remarkable features have obviously made ZIF-8 one of the most challenging MOFs. In order to understand the adsorption mechanisms of gases in ZIF-8, several crystallographic studies based on high-quality neutron powder,[12,16] synchrotron powder X-ray diffraction,[14,15] and single-crystal[13] data have been performed. These cases showed that the strongest adsorption sites on ZIF-8 were mainly associated with the MeIm linker and especially the C=C double bond of this ligand.

In the present study, we employed charge-density analysis, based on the Hansen−Coppens multipole formalism,[25] and low-temperature, high-resolution X-ray diffraction data in order to fully describe the electronic structure of the ZIF-8 framework. According to the multipole formalism, the total electron density of the crystal is described as a superposition of nonspherical pseudoatoms:

$$\rho_{\mathrm{at}}(r) = \rho_{\mathrm{core}}(r) + P_{\mathrm{val}}\kappa^{3}\rho_{\mathrm{val}}(\kappa r) + \sum_{l=0}^{l_{\max}} \kappa'^{3} R_{\mathrm{nl}}(\kappa' r) \sum_{m=0}^{l} P_{lm\pm} y_{lm\pm}(\theta, \varphi)$$

where $\rho_{\mathrm{core}}(r)$ and $\rho_{\mathrm{val}}(r)$ correspond to spherically averaged Hartree−Fock core and valence electron densities for isolated atoms, respectively. P_{val} is the electron population of the corresponding atomic valence shell, while κ and κ' are scaling parameters introduced to make valence and deformation densities expand or contract. The third term contains the sum of the angular functions $y_{lm}(\theta,\varphi)$ and describes the anisotropy of the valence density through the multipole population parameters P_{lm}. Implemented in the *XD* program package,[26] the formalism can be applied for multipole modeling of experimental and theoretical structure factors.

The total electron-density distribution determined by this approach provides a deeper understanding of the ZIF-8 properties: Topological analysis of the electron density based on the quantum theory of atoms in molecules[27] can be utilized for qualitative and quantitative evaluation of the chemical bonding in this unusually stable coordination polymer. Furthermore, by determining the boundary molecular surface at 0.001 au (0.0067 e Å^{-3}) of the ZIF-8 total electron density, one can get more exact information about the size and shape of the cavity and apertures, relevant for permeability and diffusion processes.

Another analytical tool is the electrostatic potential (EP),[28] useful for interpreting and predicting the reactivity of molecules. Because the EP has particular significance for long-range interactions, analysis of this property can help in understanding the diffusion of guest molecules within the framework. At the same time, the EP distribution on the molecular surface identifies the electrophilic or nucleophilic regions potentially suitable for guest binding. The electrostatic complementarity between molecules, which leads to their mutual recognition, has proven to be of utmost importance for interactions in biological systems[29] or crystal engineering.[30] To the best of our knowledge, this is the first charge-density study regarding not only the zeolite-type MOFs but PCPs in general. Several theoretical and experimental studies have been reported on non-PCPs.[31−33]

■ EXPERIMENTAL METHODS AND THEORETICAL CALCULATIONS

Synthesis of ZIF-8. ZIF-8 was synthesized following standard procedures based on hydrothermal solution synthesis.[2] In a 6 mL vial, a mixture of 32 mg (1.2×10^{-4} mol) of $Zn(NO_3)_2 \cdot 4H_2O$ and 10 mg (1.2×10^{-4} mol) of 2-methylimidazole was placed and dissolved in 5 mL of dry *N*,*N*-dimethylformamide (DMF). The vial was screw-capped and heated to 140 °C at a rate of 10 °C/h. The solution was kept at 140 °C for 24 h and then allowed to cool to ambient temperature slowly.

To remove the enclosed solvent from the framework the cubic-shaped ZIF-8, crystals were filtered from mother liquor, washed with portions of fresh DMF (3 × 5 mL), and stirred in methanol for 24 h. Following filtration, the colorless crystals were activated, that is, emptied from guest molecules by a vacuum of 10^{-6} mbar at 140 °C for 48 h.[34] The crystal sample was positively matched to simulation from the deposited single-crystal X-ray data file (Figure S22 in the Supporting Information, SI). From the N_2 adsorption isotherm (Figures S23−S25 in the SI with BET plots), the BET surface area was 1800 m^2 g^{-1} (lit.[2] 1630 m^2 g^{-1}) and the pore volume calculated as 0.706 cm^3 g^{-1} (lit.[2] 0.636 cm^3 g^{-1}). The pore width has a maximum at 12.5 Å (Figure S26 in the SI; lit.[2] 11.6−14.6 Å).

High-Resolution X-ray Crystallography. Up to now, 32 X-ray diffraction studies on ZIF-8 have been reported. Yet, the majority of the reported structures on ZIF-8 also include different kinds of solvents or adsorbed guest molecules. The purpose of our study was to investigate the electron-density distribution of the activated form of ZIF-8, without interference of the electron density of the guest molecules. Apart from that, there are a number of criteria that must be satisfied during the high-resolution charge-density experiment: (i) data collection should be performed at low temperature ($T \leq 100$ K); (ii) data collection should be performed at least to a sin θ/λ of 1.1 Å^{-1}; (iii) a number of observed intensities in the high-resolution region (sin $\theta/\lambda \geq 0.8$ Å^{-1}) must be sufficient in order to get accurate, unbiased structural parameters for the high-order refinement preceding the multipole refinement; (iv) high redundancy must be achieved during data collection in order to get reliable intensities for further analysis of the fine electronic properties.

The Invariom refinement applied in this study also requires high-quality diffraction data (with sin $\theta/\lambda \approx 1.0$ Å^{-1}); this approach, however, can help in the cases lacking the observed intensities at high diffraction angles, such was the case with the PCP ZIF-8. The single crystal selected for high-resolution X-ray analysis was placed in a glass capillary, which was evacuated and sealed under vacuum in order to prevent N_2 diffusion during the low-temperature diffraction experiment. In detail, the degassed ZIF-8 sample was flushed with N_2 gas. Using Schlenk techniques, a common X-ray glass capillary was placed within a Schlenk tube. One crystal was carefully selected and transferred to the capillary. A vacuum of 10^{-3} mbar was applied again for 4 h, and the capillary was sealed with a soldering device, which was inserted through a Quick-fit adapter.

The diffraction intensity sets were collected on a Bruker Kappa APEX2 CCD diffractometer equipped with a molybdenum microfocus tube and a multilayer mirror (Mo Kα radiation; $\lambda = 0.71073$ Å). A low temperature of 100.0(1) K was reached by an evaporated liquid-N_2 flux over the sealed crystal. Data collection was performed in ω-scan mode with a scan width of 0.2°. Different 2θ settings of the detector (±10, 30, −50, 70, and 75°) at a distance of 49 mm were used, yielding a maximum resolution in sin θ/λ of 1.1 Å^{-1}. Data integration was performed with *SAINT V8.27B*[35] followed by semiempirical absorption correction with *SADABS*.[36] The *SORTAV*[37] program was used for final data sorting and averaging. A total of 109942 reflections collected, with an average redundancy of 23.6, yielded 4528 unique data ($R_{int} = 4.6\%$); however, because of the low diffraction power of the microporous sample, 1911 reflections with $I > 2\sigma(I)$ were included in the refinement. The crystallographic details are given in Table 1.

Table 1. Crystal Data and Structure Refinement for ZIF-8

	expt model **m1a** with Invariom multipole refinement	high-pressure structure for model **m2**[a]
empirical formula	$(C_8H_{10}N_4Zn)_n$	$(C_8H_{10}N_4Zn)_n \cdot 3.42nCH_3OH$
fw	227.57	337.16
temperature (K)	100.0(1)	293
cryst syst	cubic	cubic
space group	$I\bar{4}3m$	$I\bar{4}3m$
unit cell dimens		
a (Å)	16.9386(8)	17.0710(17)
V (Å^3)	4860.0(4)	4974.8(9)
Z	12	12
abs coeff (mm^{-1})	1.51	1.49
D_{calc} (g cm^{-3})	0.945	1.350
cryst size (mm^3)	0.125 × 0.155 × 0.155	0.20 × 0.20 × 0.10
θ range for data collection (deg)	1.70−51.41	2.92−26.39
reflns collected	109942	14248
indep reflns [sin $\theta/\lambda \leq$ 1.0 Å^{-1}]	3226	956
no of reflns used [$I > 2\sigma(I)$]	1911	745
GOF	0.701	0.9636
R_{int}	0.0456	0.0658
final R indices		
spherical atom refinement R1, wR2 [$I > 2\sigma(I)$]	0.0201, 0.0368	0.0512, 0.1452
aspherical atom refinement R1, wR2 [$I > 2\sigma(I)$]	0.0172, 0.0205	

[a] Data from ref 23; CCDC 739165 (1.47 GPa). This data was used for multipole modeling in the *XD* program package.

CCDC 1046832 contains the supplementary crystallographic data for this paper. These data can be obtained free of charge from the Cambridge Crystallographic Data Centre via www.ccdc.cam.ac.uk/data_request/cif.

The initial multipole refinement performed with this X-ray data set appeared to not be reliable enough; this was mostly due to the insufficiency of the observed reflections in the high-resolution data range, which disabled unbiased high-order refinement. Considering the porosity of the ZIF-8 crystal structure, such behavior was expected. Nevertheless, this situation prompted us to search for alternative ways for electron-density modeling. The charge-density databases, such as UBDB,[38] ELMAM,[39] or Invariom,[40] providing transferable aspherical atomic scattering factors, have proven to be reliable for modeling of

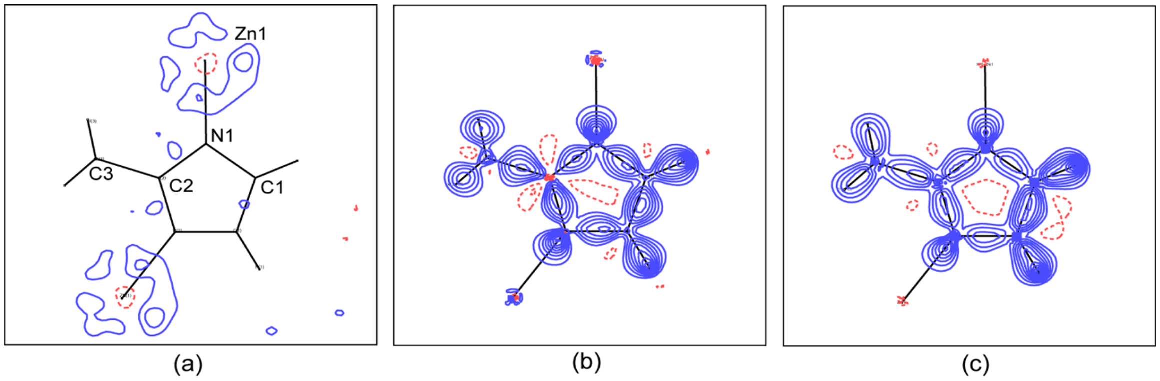

(a) (b) (c)

Figure 2. (a)Residual and (b) static electron-density maps in the plane of the MeIm linker from the Invariom model combined with experimental data, **m1a**, and (c) static electron-density map for theoretical model **m1b**. Contours are at 0.1 e Å^{-3}.

Table 2. Topological Properties of Covalent Bonds in ZIF-8[a]

bond	BP[b] (Å)	d_1[c] (Å)	ρ_{bcp}[d] (e Å^{-3})	$\nabla^2\rho_{bcp}$[e] (e Å^{-5})	ε	G_{bcp}[f] (au)	V_{bcp}[g] (au)	H_{bcp}[h] (au)
Zn−N	1.989	0.985	0.59	9.4	0.01	0.114	−0.130	−0.016
	1.989	*0.965*	*0.58*	*9.5*	*0.09*	*0.114*	*−0.130*	*−0.016*
	1.993	*0.971*	*0.56*	*9.2*	*0.08*	*0.110*	*−0.124*	*−0.014*
N−C1	1.380	0.767	2.20	−15.8	0.21	0.335	−0.833	−0.498
	1.379	*0.787*	*2.03*	*−13.3*	*0.15*	*0.296*	*−0.729*	*−0.433*
	1.384	*0.775*	*2.01*	*−11.0*	*0.11*	*0.303*	*−0.720*	*−0.417*
N−C2	1.340	0.769	2.36	−24.0	0.27	0.333	−0.916	−0.582
	1.340	*0.771*	*2.21*	*−16.6*	*0.20*	*0.333*	*−0.838*	*−0.505*
	1.335	*0.762*	*2.26*	*−17.2*	*0.18*	*0.345*	*−0.868*	*−0.523*
C1−C1′	1.366	0.683	2.20	−22.7	0.20	0.285	−0.805	−0.520
	1.361	*0.681*	*2.18*	*−18.0*	*0.35*	*0.312*	*−0.811*	*−0.499*
	1.331	*0.665*	*2.26*	*−19.2*	*0.33*	*0.331*	*−0.861*	*−0.530*
C2−C3	1.494	0.763	1.78	−13.7	0.04	0.216	−0.575	−0.358
	1.494	*0.764*	*1.66*	*−9.7*	*0.11*	*0.211*	*−0.523*	*−0.312*
	1.501	*0.766*	*1.61*	*−8.4*	*0.05*	*0.204*	*−0.495*	*−0.291*
C1−H1	1.031	0.675	2.02	−24.1	0.04	0.217	−0.684	−0.467
	1.031	*0.675*	*2.02*	*−20.3*	*0.09*	*0.243*	*−0.697*	*−0.454*
	1.031	*0.678*	*2.00*	*−19.0*	*0.09*	*0.247*	*−0.691*	*−0.444*
C3−H2	1.030	0.631	2.07	−26.7	0.02	0.216	−0.709	−0.493
	1.030	*0.667*	*1.96*	*−17.6*	*0.03*	*0.244*	*−0.671*	*−0.427*
	1.030	*0.687*	*2.00*	*−18.7*	*0.00*	*0.248*	*−0.690*	*−0.442*
C3−H3	1.027	0.627	2.08	−27.1	0.02	0.215	−0.710	−0.495
	1.026	*0.667*	*2.00*	*−18.7*	*0.04*	*0.248*	*−0.690*	*−0.441*
	1.027	*0.682*	*1.98*	*−18.1*	*0.02*	*0.248*	*−0.683*	*−0.435*

[a] The first value in the row corresponds to **m1a**; the second and third values, in italics, correspond to **m1b** and **m2**, respectively. The BCP parameters for **m1c** are nearly identical with those for **m1b** and, hence, are given in the SI (Table S2). Atom numbering:

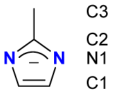

[b] Bond path length. [c] Distance of the BCP to the nuclei of the first atom in the column. [d] Electron density in BCP. [e] Laplacian value of the electron density in BCP. [f] Kinetic energy densities. [g] Potential energy densities. [h] Total energy densities.

large molecular and macromolecular structures. We decided to employ Invariom-based structure refinement, which in the case of ZIF-8 built the density model with good fitting to the experimental X-ray diffraction data (Table 1 and Figure 2). For the Invariom procedure, we used the diffraction data up to a resolution sin θ/λ of 1.0 Å^{-1} (data completeness of 90.2%). It should be mentioned that the overall completeness of the data collected for a resolution sin θ/λ of up to 0.8 Å^{-1} was 100%. The Invariom refinement has been successfully used previously for electron-density modeling of different molecular systems.[41]

Methodology of Charge-Density Analysis. The crystal structure of ZIF-8 was solved by direct methods using *SHELXS-97*[42] and refined by full-matrix least squares on F^2 using *SHELXL-97*.[42] The resulting independent atom model (IAM) was imported into the *XD2006* program package[26] for multipole refinement. After the initial spherical refinement, C−H bond distances were extended and kept fixed to the values reported from the neutron diffraction study of ZIF-8 at 3.5 K.[12] Nonspherical scattering factors of the Invariom database were then assigned to the atoms of the MeIm linker of ZIF-8. The introduction of Invariom multipole populations to the atoms of the MeIm linker led to a substantial improvement of the density model and the subsequent refinement of conventional parameters (x, y, z, and U_{ij}) against X-ray diffraction data, resulting in much better figures of merit. The Invariom database, however, does not contain information about the electronic properties of metal ions. To model the Zn atom in the case of ZIF-8, only the 4s electrons were included in the Zn valence shell, while the d^{10} electrons were included in the core and kept unperturbed. Several accurate charge-density studies established the relevance of this model for the Zn atom placed in a tetrahedral environment.[43] Finally, to take into account the possible charge transfer between Zn and the MeIm linker, the monopole populations of all atoms have been refined in the subsequent least-squares cycles to full convergence. The final residual density map (Figure 2a), based on the experimental data set up to a resolution of 1.0 Å^{-1}, confirmed the suitability of the approach. The residual density in the region of the MeIm ring is essentially featureless, while the maximal residual peaks, up to 0.27 e Å^{-3}, can be found in the vicinity of the Zn atom. Figure 2b also shows the resulting static density map in the plane containing the Zn-MeIm unit.

The described Invariom-based model combined with experimental data will hereafter be assigned as model 1a (**m1a**). To complement the conclusions drawn for **m1a**, we performed an additional charge-density refinement on the same ZIF-8 geometry using the theoretical structure factors from periodic quantum-mechanical calculations by *CRYSTAL09*[44] (model 1b, **m1b**). The *CRYSTAL* code has been previously confirmed as successful in the description of the electronic properties of MOFs[32] and coordination polymers.[31a] The good agreement in the electron-density distribution of **m1a** and **m1b** (Figure 2b,c) motivated us to further extend our investigation on ZIF-8 by involving two additional theoretical models.

Analysis of the crystal structures on ZIF-8 contained by Cambridge Structural Databank (CSD)[45] (Refcodes: FAWCEN02, FAWCEN03, GITSUY, MECWEX, OFERUN03, TUDHUW, TUDJAE, TUDJEI, TUDJIM, TUDJUY, TUDKAF, TUDKEJ, VELVOY, SEFTOO, SEFTUU, and SEFVAC) put our attention on the fact that the authors reported mainly two orientations of the methyl group of the MeIm linker (Figure S1a,b in the SI). In **m1a** and **m1b**, the orientation and C−H distances of the methyl group (Figure S1a in the SI) were all fixed to the geometry reported in the neutron study on ZIF-8 at 3.5 K.[12] With a goal to test the influence of different orientations of the methyl group on the general electrostatic properties of ZIF-8, we introduced model 1c (**m1c**), differing in geometry from those of **m1a** and **m1b** only in the methyl group orientation (Figure S1b in the SI).

Finally, to analyze the changes in the electrostatic and topological properties in ZIF-8 induced by linker reorientation (Figure S1c in the SI), we also introduced the theoretical charge-density analysis on the "high-pressure" structure, reported by Moggach et al.,[23] which is hereafter denoted as model 2 (**m2**).

Computational Details. Single-point periodic quantum-mechanical calculations have been performed with the *CRYSTAL09* package[44] using the periodic density functional theory (DFT) with the B3LYP functionals.[46] The basis set used in the calculations was 6-31G** for N, C, and H atoms,[47] while pob-TZVP was used for the Zn atom.[48] The theoretical structural factors calculated for **m1b**, **m1c**, and **m2** to a resolution of 1.2 Å^{-1} (Table S1 in the SI) were further used for multipole modeling in the *XD* program package.[26] The details of multipole refinement are given in the SI.

RESULTS AND DISCUSSION

Topological Features of ZIF-8. The topological properties of covalent bonds from the different models, **m1a**, **m1b**, and **m2**, are listed in Table 2. For **m1c**, differing from **m1b** only in the methyl group orientation, the topological parameters are listed in Table S2 in the SI. The spatial distribution of bond critical points (BCPs) in all models is similar, as shown by molecular graphs in Figure S2a in the SI. The electron density (ρ_{bcp}) and Laplacian ($\nabla^2\rho_{\mathrm{bcp}}$) values show the same trends and correlate well with the lengths of the bond paths (BPs). The imidazole bonds show typical features of the shared shell interactions, which are expressed by the high values of ρ_{bcp}, the negative values of $\nabla^2\rho_{\mathrm{bcp}}$, and the negative values of the total energy density (H_{bcp}).[49] For two polar N−C bonds, the positions of the BCPs are shifted toward the less electronegative atom (Figure S2a in the SI). The value of ρ_{bcp} and ellipticity (ε) are somewhat higher for the N−C2 bond in comparison to the N−C1 bond, suggesting a more pronounced double-bond character in the case of the former. The amount of ρ_{bcp} contained by the C1−C1′ bond is also substantial, with high ellipticity reflecting the double-bond character; this is in contrast to the C2−C3 bond, which is a typical single bond.

It is interesting to compare the topological properties of **m1**, corresponding to the "ambient-pressure" structure of ZIF-8, to those of the "high-pressure" structure[23] **m2**, which differ in the orientation of the MeIm linker (Figures 1 and S1 in the SI). We put more attention on the Zn−N bond, which is considered as the place relevant for linker reorientation. The Zn−N bonds in **m1** and **m2** have similar lengths of 1.9892(7) and 1.993 Å. The BCPs are located directly on the bond axes, and none of the BPs is curved (Figure S2a in the SI). The BCPs in the Zn−N bonds have low ρ_{bcp} values, positive values of $\nabla^2\rho_{\mathrm{bcp}}$, and small negative values of H_{bcp}, which is characteristic for metal−ligand coordination bonds. These parameters are slightly higher in **m1** in comparison to **m2**, suggesting a somewhat stronger coordination bond in the former complex. To better reveal the character of the Zn−N bond, changes in the density and Laplacian profiles are monitored along the corresponding BPs and compared with the profiles in nonbonded systems, i.e., the IAMs. Inspection of the profiles in Zn−N for **m1** and **m2** indicates a behavior very similar to the one recently described for the Zn−O bonds of a Zn-containing coordination polymer,[31a] which were characterized as both electrostatic and covalent in nature. Details of the profile analysis for the Zn−N bond are included in the SI (Figures S4 and S5). Here we report that changes in the profiles compared to reference IAMs (with a focus on the electron density along the Zn−N BP and the charge concentration from the N-donor atom directed toward the Zn atom) are more pronounced in **m1**.

The topology of Laplacian map for the N-donor atoms shows that in all models the valence shell charge concentration (VSCC) pointing in the direction of the Zn atom is higher than two others toward the neighboring C atoms (Table S3 in the SI). The Laplacian maps in the plane of the MeIm ring do not reveal the particular differences between the different models (Figure S2b in the SI). The projection orthogonal to the MeIm ring and containing the Zn−N bond, however, shows that the VSCC of the N-donor atom in **m2** lies somewhat outside the direction of the bond vector (Figure S2c in the SI). This observation suggests the existence of strain in the **m2** form, which could be considered as one of the factors assisting the reversible ligand reorientation between ZIF-8 forms **m1** and **m2**. Here we add that the values of the total energies obtained by the theoretical calculation (*CRYSTAL09*[44]) for crystal systems of **m1b** and **m2** differ by only 3.1 kcal/mol.

Dimensions of ZIF-8 Apertures and Cavities Determined from the Electron-Density Distribution. As mentioned above, the ZIF-8 cage has eight SM and six FM apertures (cf. Figure 1). In the analysis of the diffusion and permselectivity of ZIF-8, the advantage is given to the SM apertures because of their larger size. From the results of the classical X-ray diffraction experiments,[1,2] the effective size of the SM apertures was estimated as 3.4 Å. Recent analysis on the kinetic uptake of short alkanes[18] indicated larger dimensions of 4.0−4.2 Å, taking also into account the aperture flexibility. For static structures, the aperture is a median value that does not take into account the lattice vibrations of the framework, which

Table 3. Dimensions of ZIF-8 Apertures[a] at 0.001 and 0.005 au Total Electron Density

		m1b		**m1c**		**m2**	
boundary value (au)		SM	FM	SM	FM	SM	FM
0.001	*P* (Å^2)[b]	5.93	1.51	5.93	2.35	9.56	4.77
	d, *l* (Å)	2.75, 4.60	1.38, 1.90	2.75, 4.60	1.73, 2.40	3.49, 5.0	2.45, 3.40
0.005	*P* (Å^2)[b]	9.87	5.32	9.87	6.05	14.10	9.11
	d, *l* (Å)	3.54, 5.60	2.60, 4.40	3.54, 5.60	2.78, 4.40	4.24, 5.60	3.41, 4.80

[a] SM = six-membered, hexagonal aperture. FM = four-membered, square aperture. Compare Figure 1c. [b] *P* = area of the circle; *d* = diameter of the circle; *l* = longest dimension of the aperture.

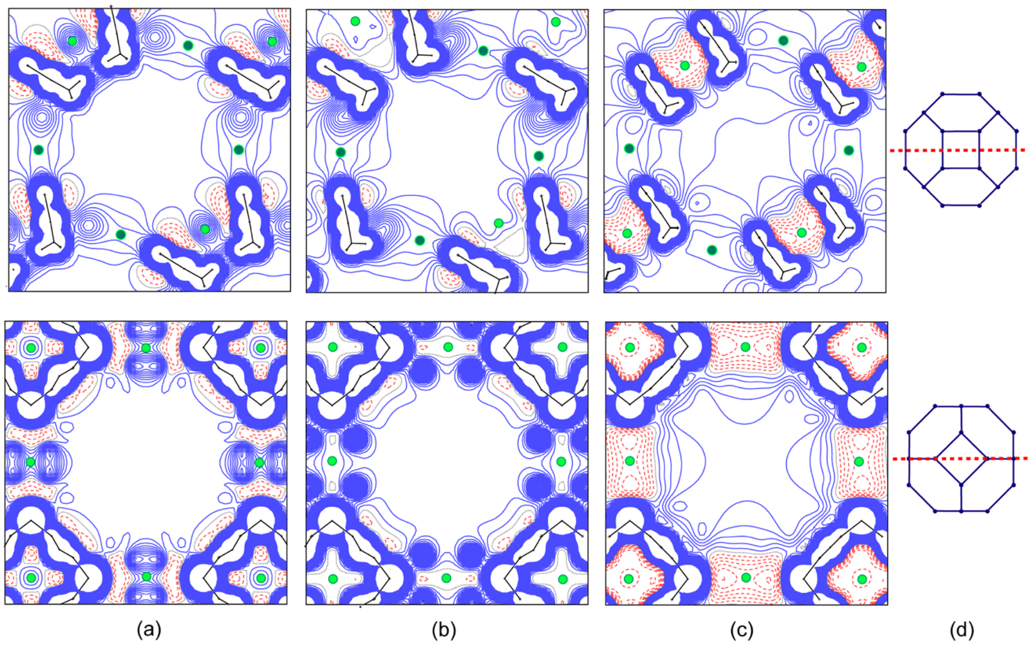

Figure 3. EP projected in two planes of **m1b** (a), **m1c** (b), and **m2** (c) cutting the corresponding β cage (see Figure 1c), as indicated by the dashed red line in part d. The upper plane bisects the β cage through the centers of two opposite FM apertures and the centers of four neighboring SM apertures; the lower plane bisects the β cage through the centers of four FM apertures. Positive and negative isopotential lines are given in blue and red, respectively. Contours are at ±0.01 au. The circles in light and dark green indicate the centers of the SM and FM apertures, respectively. The EP projections in two additional planes passing through the volume and center of the β cage are given in Figure S16 in the SI.

often strongly affect the effective pore size. Here we examine the dimensions of the apertures on the basis of the electron-density distribution in the ZIF-8 structure. The aperture sizes are measured on the boundary value of 0.001 au of the total electron density and also at the value of 0.005 au, which is still considered to be a relatively low concentration of the electron density. To be able to compare on the same grounds the fine changes in the boundary electron density of the apertures caused by the methyl group (**m1c**) or linker reorientation (**m2**), Table 3 lists dimensions from three equivalently obtained theoretical models.

For both **m1** and **m2**, the density surrounding the SM apertures has a rather irregular shape (Figure S7 in the SI). With the aim to rationally estimating and comparing the abilities of the SM apertures for molecule diffusion, we applied a rather restrictive approximation to the aperture effective surface by confining it to the surface of a circle. The areas of the corresponding circles are given in Table 3, together with the longest dimension of the aperture. The additional dimensions can be found in Figures S7−S11 in the SI. These data indicate that the accessible SM aperture area increases up to 62% during the reorientation of the MeIm linker and the transition from the **m1** form to the **m2** form. For molecules more globular in shape, the diameter of 3.5 Å could be considered as a limiting dimension. Although the largest dimension of the aperture can exceed 5 Å, the area outside of the circle is significantly narrower and, at 0.001 au in **m2**, reaches only 1.4 Å in width (Figures S7−S11 in the SI).

In all models, the surface of the FM apertures can also be approximated to the circular shape. As expected, at a density value of 0.001 au,[27] FM apertures are significantly smaller than SM apertures. It should be noticed, however, that at a somewhat higher electron-density concentration of 0.005 au the area of the FM aperture increases over 2.5 times (in **m1b**) in contrast to that of the SM aperture, which increases by 68%. This is due to the fact that the bordering density confining the SM apertures belongs to closely surrounding H atoms, which limit the size of the SM aperture by the position of their nuclei (the closest H···H distances are 3.0 and 3.8 Å in **m1** and **m2**, respectively). On the other hand, the bordering density of the FM apertures is formed of π electron density, which could be considered as "softer" and more flexible for spatial rearrangement in comparison to the density of the SM apertures. The closest separation between the surrounding N atoms is 6.5 Å in all models and appears sufficiently large (for the molecule entry) with regard to the closest distances in the SM apertures (the closest non-H atom; i.e., the C···C distances are 5.0 and 3.5−5.6 Å in **m1** and **m2**, respectively). This result suggests

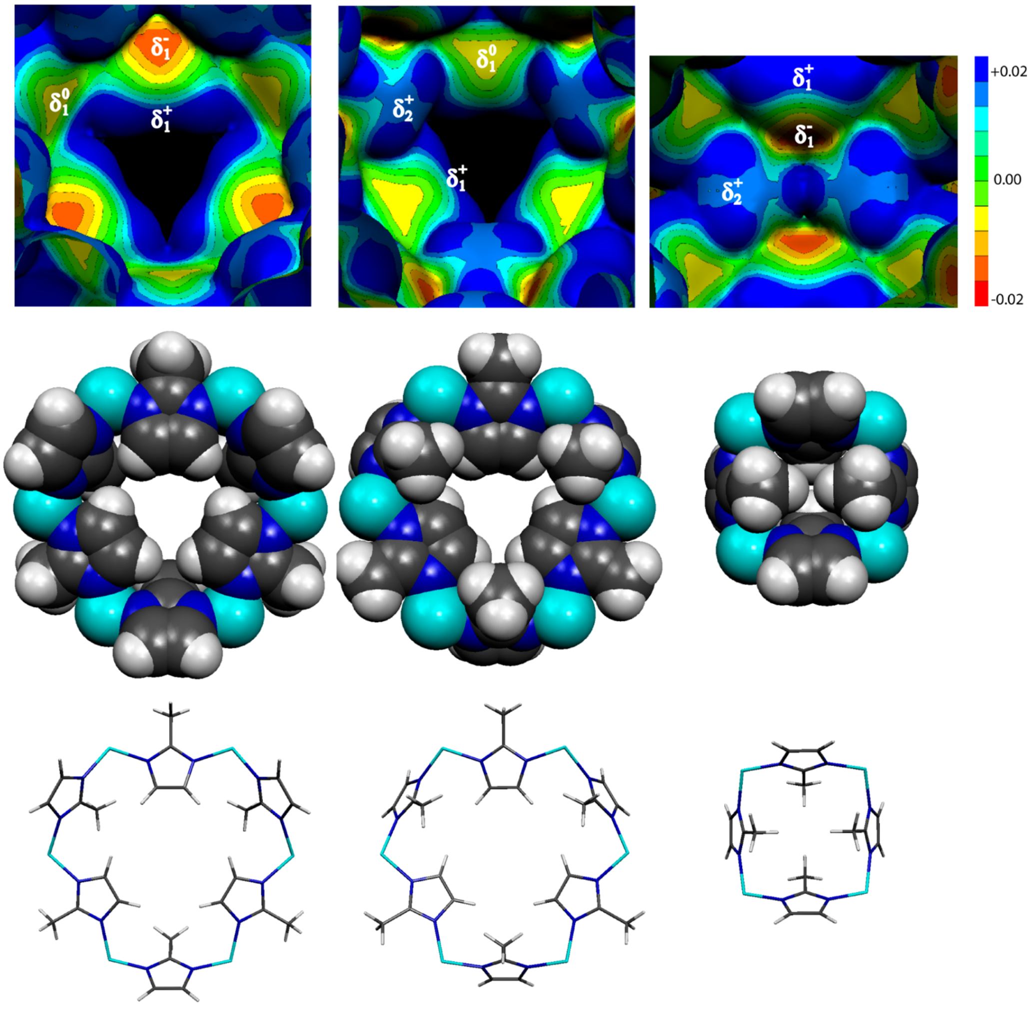

(a) (b) (c)

Figure 4. 3D representation of the EP on the molecular surface (0.001 au) surrounding the two sides of the SM (a and b) and FM (c) apertures in **m1b**. A comparison with the EP distribution in **m2** is given in Figure S14 in the SI;[50] δ^+, δ^-, and δ^0 indicate the distinct regions with positive, negative, and neutral EP, respectively.

that, despite the apparently smaller size, the FM apertures could also have a significant role in guest molecule diffusion. This is particularly true for **m2**, where reorientation of the MeIm ring (and consequent displacement of the methyl groups; Figures S7c and S12 in the SI) completely opens the channel entrance through the FM aperture. In fact, the area of the FM aperture in **m2** approaches in size the area of the SM aperture determined for **m1** (Table 3). An advantage of the FM aperture in **m2** is the uniform cylindrical shape for guest molecule diffusion.

The total electron density defining the wall of the ZIF-8 cavity has a rather irregular shape, as presented in Figure S13 in the SI. Apart from enlargement of the apertures, reorientation of the MeIm linkers brings little change in the effective dimension of the cavity. The longest and shortest diameters estimated for the **m1** (**m2**) cavity are 14.4 (13.8) and 11.7 (11.4) Å, while the surface area of the largest plane passing the cavity is 142.5 (127.1) Å^2.

EP Distribution within the ZIF-8 Frameworks. On the basis of the electron-density distribution, we further derived the properties of EP,[28c,d] keeping in mind that the long-range electrostatic forces (as "driving forces") would primarily affect the guest molecule entering and moving within the ZIF-8 framework. We observed, however, that even small structural changes such as the methyl group reorientation, which in the case of the discrete molecular structures would not imply significant EP differences, in the case of ZIF-8 induce substantial changes in the electrostatic properties (Figure 3a vs Figure 3b). This can be related to the cubic crystal symmetry with only one unique MeIm ligand in the asymmetric unit, which imposes the orientation of adjacent MeIm ligands. If the high symmetry of this "supermolecule" is preserved on the microscopic molecular level, then the methyl groups come into close proximity, leading to a cooperative, cumulative effect with amplified electrostatic properties. For the same reason, more significant conformational changes such as reorientation of the imidazole linkers introduce tremendous changes in the electrostatic properties of ZIF-8, with obvious consequences for the apertures as well as the cavity. This is well illustrated by the mapping of EP in the equivalent planes passing through the cavity volumes of the **m1** and **m2** structures (Figure 3).

For a more detailed description of the inner electrostatic properties of the cavity, we employed a 3D projection of EP on the isodensity surfaces (0.001 au) of **m1** and **m2** (Figures 4 and S14 in the SI, respectively). In **m1**, the inner electrostatic properties of the cavity are examined in terms of the individual properties of the apertures constructing the cavity, as given in

Figure 4. Here it should be noticed that, viewed from inside the β cage, the cavity wall contains a single type of the six FM apertures (Figures 4c and S6a in the SI), while there are two different types for the eight SM apertures, that is, four each[51] (Figures 4a,b and S6b in the SI). The latter introduces additional diversity in the EP features on the overall surface of the cavity. The region surrounding the entrance through the SM aperture has positive EP (+0.05 au) originating from MeIm C−H fragments (region denoted with δ_1^+ in Figure 4) as well as vicinal methyl H atoms (δ_2^+ in Figure 4). In contrast, the FM aperture can be considered as dominated by negative EP (up to −0.02 au) because of the π electron density of four closely positioned imidazole rings. Two sides of the imidazole ring display somewhat different EP values depending on whether they are directed toward the FM aperture (δ_1^- in Figure 4) or toward an annelated SM aperture (δ_1^0 in Figure 4). Each type of the two latter EP surfaces appears above the SM aperture and makes its two sides dissimilar, as mentioned above (Figure 4a,b).

In a global view, the surface of the cavity contains a number of small regions with moderate EP in the range of +0.05 to −0.02 au. The diversity of EP within the cavity is well illustrated with 2D maps in Figure 3. The two projections in the planes passing through the FM apertures and the center of the cavity show frequent alternation of the regions with weakly positive, neutral, and weakly negative EP (see Figure S16 in the SI for further details). Taking into account the multiplication by symmetry, one can count 38 clearly separated regions of different EPs on the cavity surface. More specifically, one cavity displays 14 regions of positive EP ($8\delta_1^+$ and $6\delta_2^+$; Figure 4), 12 regions of negative EP ($12\delta_1^-$; Figure 4), and 12 regions of negative to neutral EP ($12\delta_1^0$; Figure 4). EP generated in the center of the cavity is slightly positive (+0.016 au) and spreads in a symmetrical octahedral shape toward the FM apertures on the cavity wall. One can expect that such a weak EP, which takes approximately half of the cavity volume, would facilitate the diffusion within and the transfer of guest molecules from one to another binding site. Further information on the spatial distribution of EP within the cavity can be found in Figure S17 in the SI. It is interesting to note that the halves of the ZIF-8 cavity do not actually reflect each other, but they are rotated by 90° (Figure S18 in the SI). Keeping in mind the dissimilarity of the neighboring SM aperture faces (Figure 4a,b), this leads to a maximally scattered and efficient distribution of the local EPs. With such an EP distribution, exchanging in a narrow range from weakly positive to weakly negative, it is likely that the ZIF-8 cavity will be able to interact with the guest molecules by weak van der Waals interactions as well as stronger electrostatic forces. One can therefore suggest a significant electrostatic flexibility of the ZIF-8 framework, which allows either binding (reversible adsorption/desorption) of molecules different in nature (homonuclear or heteronuclear) or their easy diffusion within the framework.

In contrast to **m1**, which offers 38 regions of different EPs (Figures 3 and 4), **m2** has a much more polarized distribution of EP because it has only two different regions. Thus, in **m2**, there is only one large, continuous region of positive EP that occupies the cavity and expands to the other cavities via SM apertures (see the upper projection in Figure 3c). Another EP region is localized in the FM aperture and possesses relatively strong negative EP (Figures 3c and S14 in the SI). Specifically, the range of EP values in **m2** (−0.05 to +0.07 au) is higher than that in **m1** (−0.02 to +0.05 au), while the EP generated in the center of the **m2** cavity is more positive than that in **m1** (+0.05 in contrast to +0.016 au, respectively). From the aspect of EP, the above comparison shows that reorientation of the MeIm linkers drastically changes the EP properties of ZIF-8 either in the number of separate EP regions or in the general values. This difference is especially reflected in the area of the FM aperture, which changes from a mix of positive and weak negative EP regions (**m1**; Figure 4) to one region of relatively strong negative EP (**m2**; Figure S14a in the SI).

The above results clearly indicate that the distribution of EP in the cavity of **m1** provides an excellent ability for adsorption/storage of electrostatically very different molecules. Namely, the cavity of **m1** possesses 38 nucleophilic and electrophilic regions, which are arranged in an alternate manner. The size of the regions and their mutual arrangement enable the surface of the **m1** cavity to accommodate any small molecule on the basis of electrostatic complementarity. In other words, any small molecule using its own (analogous) electrostatic requirement can find a suitable area at the cavity surface or above it, i.e., before direct contact of the van der Waals surfaces. This electrostatic flexibility of **m1** is especially increased by considering also a partial reorientation of the MeIm linkers (one or more depending on a particular need) as an adjustment to the specific electrostatic requirement of the diffusing molecule. The existence of regions with negative EP in **m1** is particularly important because all small molecules (except anions) usually have large regions of positive EP and small regions of negative EP (for example, almost all C−H groups have positive EP at the molecular surface or beyond). Hence, the overall positive EP observed in the cavity of **m2**, in contrast to **m1**, can assist the desorption of molecules from the surface and their further diffusion to neighboring cavities. The latter does not apply to the anionic species, which can find **m2** very proper for adsorption. It is important to keep in mind that **m1** and **m2** represent only two limiting states of the dynamic ZIF-8 system; therefore, we can suggest that by changing the MeIm tilt angle this MOF is able to generate a number of other intermediary states displaying a range of EP topologies.

Regardless of the complexity of the proposed mechanism and the changeable EP features, we have searched for the possible correlation between the inner electrostatic structure of ZIF-8 and the preferential adsorption sites reported in previous studies. In general, the effects of EP on adsorption can be revealed through the mutual recognition of components (framework and guest molecules), which follows the principals of electrostatic complementarily between their differently charged fragments. The clear evaluation of the EP influence on homonuclear gases such are H_2, N_2, or I_2 is, however, somewhat difficult because of the nonpolar nature of these molecules. Nevertheless, in studies on the H_2 binding affinities,[52,53] it is highlighted that the existence of partial charges, either positive or negative, on the MOF surface can strengthen the binding of H_2 through dipole−induced dipole interactions. In that context, the above analysis of the electrostatic properties confirms that the **m1** form of the ZIF-8 framework (displaying frequent alternation and maximal dispersion of partial charges) undeniably fulfills this requirement. Figure S19 in the SI displays 2D maps of EP with the reported binding positions of the D_2[12] and N_2[13] molecules with respect to EP of the ZIF-8 framework. On the other hand, the cases in which some initial polarity exists in the bonds of guest molecules, such is heteronuclear CD_4, give more indication about the possible role of EP. Thus, in the primary binding site of CD_4, which was determined experimentally,[16] the adsorbed molecule is placed between three imidazole rings, with the D atoms clearly oriented toward the regions of neutral and weekly negative EP (Figure S20 in the SI).

■ CONCLUSIONS

In conclusion, on the basis of experimental and theoretical structure factors, we have determined and analyzed the electron-density distribution within the PCP ZIF-8 (**m1**). Taking into account the structural and conformational changes, which eventually lead to the "high-pressure" form of ZIF-8 (**m2**), we have also investigated their impact on the local and global electronic and electrostatic features of the system.

The two limiting forms of ZIF-8 (**m1** and **m2**) show small differences in the topology of the electron density. The investigation of the size of the apertures from the aspect of the total electron density (at 0.001 au) puts forward the FM apertures as an additional trajectory important for molecular diffusion. Especially in form **m2** of ZIF-8, the effective area of the FM apertures approaches in size the area of the SM apertures determined for **m1**. Further widening of the FM channel can be expected when taking into account the potential flexibility of π-electron clouds surrounding the FM aperture and rotation of the methyl group of the linker.

The structural changes of ZIF-8 through reorientation of the methyl group and, particularly, reorientation of the MeIm linker have a major impact on the EP properties. The effects are multiplied by the high symmetry of the ZIF-8 cavity and are substantially increased because of the proximity of the MeIm fragments (cumulative effect). In general, the cavity of **m1** displays numerous small, well-defined regions of moderately positive, negative, and neutral EP (−0.02 to +0.05 au), which suggests the ability of ZIF-8 to engage molecules different in nature and polarity. Weak, octahedrally distributed, positive EP, which takes half of the cavity volume, allows easy diffusion and transfer of the guest molecules from one to another binding site of **m1**.

On the other hand, the cavity in **m2** displays a polarized distribution of EP, with negative EP (−0.05 au) localized within the open channels of the FM apertures, and positive EP taking all of the cavity surface (up to +0.07 au). The EP generated in the center of the **m2** cavity is also more positive than that in **m1**. Considering that the linker reorientation is a dynamic process, where **m1** and **m2** represent two limiting states, one can expect a number of intermediary structures displaying different electrostatic states, that is, different distributions of EP from neutral to moderately polar to highly polar. Such behavior indicates an electrostatic flexibility of ZIF-8, i.e., its ability to respond and to adjust to the requirement of different guest molecules in order to facilitate their diffusion or binding. Because in the case of ZIF-8 the electrostatics closely follow the structural changes, one can also hypothesize that this tight relationship puts the system in motion.

The cumulative effect observed in ZIF-8, where the small structural and local electrostatic changes result in important changes of the global electrostatic properties, could also be considered for other (high-symmetry) MOFs; accordingly, for other MOFs displaying some degree of conformational freedom, a similar mechanism of action could be proposed. Finally, it should be mentioned that the described sensitivity of the electrostatic properties and the need for high-resolution experimental data seemed initially to imply difficulties in experimental charge-density refinement and analysis of ZIF-8. It is likely that these kinds of obstacles will appear in further studies on porous MOF (especially those crystallizing in highly symmetrical, acentric space groups), which generally lack high-angle reflection data. Our findings show that the employment of charge-density databases based on the transferability concept, such as Invariom, could be a proper and reliable approach to overcoming this difficulty and extracting the valuable information concerning the charge-density distribution in this important class of porous compounds.

■ ASSOCIATED CONTENT

Ⓢ Supporting Information

X-ray crystallographic data in CIF format, details of ZIF-8 multipole modeling based on theoretical structure factors, molecular graphs and Laplacian maps for different ZIF-8 models, total electron density in the vicinity of apertures, details of the spatial EP distribution, IR spectrum, powder X-ray diffraction data, N_2 adsorption isotherm, and NL-DFT pore-size distribution curve. The experimental X-ray structure **m1a** with Invariom multipole refinement has been deposited as CCDC 1046832 with the Cambridge Crystallographic Data Centre, from which it can be obtained upon request at www.ccdc.cam.ac.uk/data_request/cif. This material is available free of charge via the Internet at http://pubs.acs.org.

■ AUTHOR INFORMATION

Corresponding Authors

*E-mail: snovak@vin.bg.ac.rs.
*E-mail: goranb@vin.bg.ac.rs.
*E-mail: janiak@uni-duesseldorf.de.

Notes

The authors declare no competing financial interest.

■ ACKNOWLEDGMENTS

S.B.N. and C.J. are grateful to the Deutsche Forschungsgemeinschaft (DFG) for Grant Ja466/30-1 fostering the international collaboration between Serbia and Germany. In part, the project was also supported by DFG Grant Ja466/25-1 and by the University of Düsseldorf through its strategic research fund (SFF). S.B.N., G.A.B., and D.F. thank the Ministry of Education and Science of the Republic of Serbia (Projects 172014 and 172035) for financial support.

■ REFERENCES

(1) Huang, X.-C.; Lin, Y.-Y.; Zhang, J.-P.; Chen, X.-M. *Angew. Chem., Int. Ed.* **2006**, *45*, 1557−1559.

(2) Park, K. S.; Ni, Z.; Cote, A. P.; Choi, J. Y.; Huang, R.; Uribe-Romo, F. J.; Chae, H. K.; O'Keeffe, M.; Yaghi, O. M. *Proc. Natl. Acad. Sci. U.S.A.* **2006**, *103*, 10186−10191.

(3) Phan, A.; Doonan, C. J.; Uribe-Romo, F. J.; Knobler, C. B.; O'Keeffe, M.; Yaghi, O. M. *Acc. Chem. Res.* **2010**, *43*, 58−67.

(4) Li, J. R.; Kuppler, R. J.; Zhou, H. C. *Chem. Soc. Rev.* **2009**, *38*, 1477−1504.

(5) Tran, U. P. N.; Le, K. K. A.; Phan, N. T. S. *ACS Catal.* **2011**, *1*, 120−127.

(6) Pan, Y.; Lai, Z. *Chem. Commun.* **2011**, *47*, 10275−10277.

(7) Lu, G.; Hupp, J. T. *J. Am. Chem. Soc.* **2010**, *132*, 7832−7833.

(8) Chen, B.; Yang, Z.; Zhu, Y.; Xia, Y. *J. Mater. Chem. A* **2014**, *2*, 16811−16831.

(9) Zhang, J.-P.; Zhu, A.-X.; Lin, R.-B.; Qi, X.-L.; Chen, X.-M. *Adv. Mater.* **2011**, *23*, 1268−1271.

(10) Assfour, B.; Leoni, S.; Seifert, G. *J. Phys. Chem. C* **2010**, *114*, 13381−13384.

(11) Wang, B.; Côté, A. P.; Furukawa, H.; O'Keeffe, M.; Yaghi, O. M. *Nature* **2008**, *453*, 207−211.

(12) Wu, H.; Zhou, W.; Yildirim, T. *J. Am. Chem. Soc.* **2007**, *129*, 5314−5315.

(13) Zhang, J.-P.; Zhu, A.-X.; Chen, X.-M. *Chem. Commun.* **2012**, *48*, 11395−11397.

(14) Fairen-Jimenez, D.; Moggach, S. A.; Wharmby, M. T.; Wright, P. A.; Parsons, S.; Düren, T. *J. Am. Chem. Soc.* **2011**, *133*, 8900−8902.

(15) Sava, D. F.; Rodriguez, M. A.; Chapman, K. W.; Chupas, P. J.; Greathouse, J. A.; Crozier, P. S.; Nenoff, T. M. *J. Am. Chem. Soc.* **2011**, *133*, 12398−12401.

(16) Wu, H.; Zhou, W.; Yildirim, T. *J. Phys. Chem. C* **2009**, *113*, 3029−3035.

(17) Li, K.; Olson, D. H.; Seidel, J.; Emge, T. J.; Gong, H.; Zeng, H.; Li, J. *J. Am. Chem. Soc.* **2009**, *131*, 10368−10369.

(18) Zhang, C.; Lively, R. P.; Zhang, K.; Johnson, J. R.; Karvan, O.; Koros, W. J. *J. Phys. Chem. Lett.* **2012**, *3*, 2130−2134.

(19) Fairen-Jimenez, D.; Galvelis, R.; Torrisi, A.; Gellan, A. D.; Wharmby, M. T.; Wright, P. A.; Mellot-Draznieks, C.; Düren, T. *Dalton Trans.* **2012**, *41*, 10752−10762.

(20) Pérez-Pellitero, J.; Amrouche, H.; Siperstein, F. R.; Pirngruber, G.; Nieto-Draghi, C.; Chaplais, G.; Simon-Masseron, A.; Bazer-Bachi, D.; Peralta, D.; Bats, N. *Chem.—Eur. J.* **2010**, *16*, 1560−1571.

(21) Liédana, N.; Galve, A.; Rubio, C.; Téllez, C.; Coronas, J. *ACS Appl. Mater. Interfaces* **2012**, *4*, 5016−5021.

(22) Saint Remi, J. C.; Rémy, T.; Hunskerken, V. V.; van de Perre, S.; Duerinck, T.; Maes, M.; De Vos, D.; Gobechiya, E.; Kirschhock, C. E. A.; Baron, G. V.; Denayer, J. F. M. *ChemSusChem* **2011**, *4*, 1074−1077.

(23) Moggach, S. A.; Bennett, T. D.; Cheetham, A. K. *Angew. Chem., Int. Ed.* **2009**, *48*, 7087−7089.

(24) Brandenburg, K.; Putz, H. *Diamond: crystal and molecular structure visualization*, version 3.2; Crystal Impact: Bonn, Germany, 2007−2012.

(25) (a) Hansen, N. K.; Coppens, P. *Acta Crystallogr.* **1978**, *A34*, 909−921. (b) Coppens, P. *X-ray charge density and chemical bonding*; Oxford University Press: Oxford, U.K., 1997. (c) Koritsanszky, T. S.; Coppens, P. *Chem. Rev.* **2001**, *101*, 1583−1627.

(26) Volkov, A.; Macchi, P.; Farrugia, L. J.; Gatti, C.; Mallinson, P.; Richter, T.; Koritsanszky, T. *XD2006: A Computer Program Package for Multipole Refinement, Topological Analysis of Charge Densities and Evaluation of Intermolecular Energies from Experimental and Theoretical Structure Factors*; 2006.

(27) Bader, R. F. W. *Atoms-in-Molecules: A Quantum Theory*; Clarendon Press: Oxford, U.K., 1990.

(28) (a) Politzer, P.; Truhlar, D. G. *Chemical Applications of Atomic and Molecular Electrostatic Potentials*; Plenum: New York, 1981. (b) Politzer, P.; Murray, J. S. *Theor. Chem. Acc.* **2002**, *108*, 134−142. (c) Ghermani, N.-E.; Bouhmaida, N.; Lecomte, C. *Acta Crystallogr., Sect. A* **1993**, *49*, 781−789. (d) Bouhmaida, N.; Ghermani, N.-E.; Lecomte, C.; Thalal, A. *Acta Crystallogr., Sect. A* **1997**, *53*, 556−563.

(29) Muzet, N.; Guillot, B.; Jelsch, C.; Howard, E.; Lecomte, C. *Proc. Natl. Acad. Sci. U.S.A.* **2003**, *100*, 8742−8747.

(30) Bogdanović, G. A.; Novaković, S. B. *CrystEngComm* **2011**, *13*, 6930−6932.

(31) (a) Jørgensen, M. R. V.; Cenedese, S.; Clausen, H. F.; Overgaard, J.; Chen, Y.-S.; Gatti, C.; Iversen, B. B. *Inorg. Chem.* **2013**, *52*, 297−305. (b) Clausen, H. F.; Overgaard, J.; Chen, Y. S.; Iversen, B. B. *J. Am. Chem. Soc.* **2008**, *130*, 7988−7896. (c) Poulsen, R. D.; Jørgensen, M. R. V.; Overgaard, J.; Larsen, F. K.; Morgenroth, W.; Graber, T.; Chen, Y.-S.; Iversen, B. B. *Chem.—Eur. J.* **2007**, *13*, 9775−9790. (d) Poulsen, R. D.; Bentien, A.; Chevalier, M.; Iversen, B. B. *J. Am. Chem. Soc.* **2005**, *127*, 9156−9166. (e) Poulsen, R. D.; Bentien, A.; Graber, T.; Iversen, B. B. *Acta Crystallogr., Sect. A* **2004**, *60*, 382−389.

(32) Civalleri, B.; Napoli, F.; Noël, Y.; Roetti, C.; Dovesi, R. *CrystEngComm* **2006**, *8*, 364−371.

(33) Chimpri, A. S.; Macchi, P. *Phys. Scr.* **2013**, *87*, 1−9.

(34) Gee, J. A.; Chung, J.; Nair, S.; Sholl, D. S. *J. Phys. Chem. C* **2013**, *117*, 3169−3176.

(35) *SAINT*, version 8.27B; Bruker AXS Inc.: Madison, WI, 2012.

(36) Sheldrick, G. M. *SADABS 2008/1 (SADABS 2008/2)*; University of Göttingen: Göttingen, Germany, 2008.

(37) Blessing, R. H. *J. Appl. Crystallogr.* **1997**, *30*, 421−426.

(38) (a) Volkov, A.; Messerschmidt, M.; Coppens, P. *Acta Crystallogr., Sect. D* **2007**, *63*, 160−170. (b) Volkov, A.; Li, X.; Koritsanszky, T.; Coppens, P. *J. Phys. Chem. A* **2004**, *108*, 4283−4300. (c) Dominiak, P. M.; Volkov, A.; Dominiak, A. P.; Jarzembska, K. N.; Coppens, P. *Acta Crystallogr., Sect. D* **2009**, *65*, 485−499. (d) Dominiak, P.; Volkov, A.; Li, X.; Messerschmidt, M.; Coppens, P. *J. Chem. Theory Comput.* **2007**, *3*, 232−247.

(39) (a) Zarychta, B.; Pichon-Pesme, V.; Guillot, B.; Lecomte, C.; Jelsch, C. *Acta Crystallogr.* **2007**, *A63*, 108−125. (b) Pichon-Pesme, V.; Lecomte, C.; Lachekar, H. *J. Phys. Chem.* **1995**, *99*, 6242−6250. (c) Lecomte, C.; Jelsch, C.; Guillot, B.; Lagoutte, A. *J. Synchrotron Radiat.* **2008**, *15*, 202−203. (d) Jelsch, C.; Pichon-Pesme, V.; Lecomte, C.; Aubry, A. *Acta Crystallogr.* **1998**, *D54*, 1306−1318. (e) Guillot, B.; Jelsch, C.; Podjarny, A.; Lecomte, C. *Acta Crystallogr.* **2008**, *D64*, 567−588.

(40) (a) Dittrich, B.; Hübschle, C. B.; Luger, P.; Spackman, M. A. *Acta Crystallogr., Sect. D* **2006**, *62*, 1325−1335. (b) Hübschle, C. B.; Luger, P.; Dittrich, B. *J. Appl. Crystallogr.* **2007**, *40*, 623−627. (c) Dittrich, B.; Strumpel, M.; Spackman, M. A.; Koritsanszky, T. *Acta Crystallogr., Sect. A* **2006**, *62*, 217−223. (d) Dittrich, B.; Munshi, P.; Spackman, M. A. *Acta Crystallogr., Sect. B* **2007**, *63*, 505−509. (e) Dittrich, B.; Hübschle, C. B.; Holstein, J. J.; Fabbiani, F. P. A. *J. Appl. Crystallogr.* **2009**, *42*, 110−1121.

(41) (a) Dittrich, B.; Koritsanszky, T.; Volkov, A.; Mebs, S.; Luger, P. *Angew. Chem., Int. Ed.* **2007**, *46*, 2935−2938. (b) Dittrich, B.; Koritsanszky, T.; Luger, P. *Angew. Chem., Int. Ed.* **2004**, *43*, 2718−2721. (c) Kratzert, D.; Leusser, D.; Holstein, J. J.; Dittrich, B.; Abersfelder, K.; Scheschkewitz, D.; Stalke, D. *Angew. Chem., Int. Ed.* **2013**, *52*, 4478−4482. (d) Holstein, J. J.; Hübschle, C. B.; Dittrich, B. *CrystEngComm* **2012**, *14*, 2520−2531. (e) Dittrich, B.; Bond, C. S.; Kalinowski, R.; Spackman, M. A.; Jayatilaka, D. *CrystEngComm* **2010**, *12*, 2419−2423. (f) Luger, P.; Weber, M.; Hübschle, C. B.; Tacke, R. *Org. Biomol. Chem.* **2013**, *11*, 2348−2354. (g) Mebs, S.; Lüth, A.; Luger, P. *Bioorg. Med. Chem.* **2010**, *18*, 5965−5974. (h) Ghadwal, R. S.; Azhakar, R.; Pröpper, K.; Holstein, J. J.; Dittrich, B.; Roesky, H. W. *Inorg. Chem.* **2011**, *50*, 8502−8508.

(42) Sheldrick, G. M. *Acta Crystallogr.* **2008**, *A64*, 112−122.

(43) (a) Spasojevic de Biré, A.; Bouhmaida, N.; Kremenović, A.; Morgant, G.; Ghermani, N. E. *J. Phys. Chem. A* **2002**, *106*, 12170−12177. (b) Novaković, S. B.; Bogdanović, G. A.; Fraisse, B.; Ghermani, N. E.; Bouhmaida, N.; Spasojević-de Biré, A. *J. Phys. Chem. A* **2007**, *111*, 13492−13505. (c) Scheins, S.; Zheng, S.-L.; Benedict, J. B.; Coppens, P. *Acta Crystallogr.* **2010**, *B66*, 366−372.

(44) Dovesi, R.; Saunders, V. R.; Roetti, R.; Orlando, R.; Zicovich-Wilson, C. M.; Pascale, F.; Civalleri, B.; Doll, K.; Harrison, N. M.; Bush, I. J.; D'Arco, P.; Llunell, M. *CRYSTAL09*; University of Torino: Torino, Italy, 2009.

(45) Allen, F. H. *Acta Crystallogr.* **2002**, *B58*, 380−388.

(46) Lee, C. T.; Yang, W. T.; Parr, R. G. *Phys. Rev. B* **1988**, *37*, 785−789.

(47) Krishnan, R.; Binkley, J. S.; Seeger, R.; Pople, J. A. *J. Chem. Phys.* **1980**, *72*, 650−654.

(48) Peintinger, M. F.; Oliveira, D. V.; Bredow, T. J. *J. Comput. Chem.* **2013**, *34*, 451−459.

(49) Abramov, Y. A. *Acta Crystallogr., Sect. A* **1997**, *53*, 264−272.

(50) In Figure 4, we decided to represent the EP properties via the theoretical model **m1b** for direct comparison with the high-pressure theoretical model **m2** (Figure S14 in the SI).

(51) It should be noticed that, when viewed from the center of the β cage, the cavity wall contains six FM apertures with equal local electrostatic features (Figure 4c). Unlike the symmetrical FM aperture, the SM aperture is asymmetrical with respect to the middle plane (passing through the surrounding Zn atoms; Figure S6 in the SI); hence, two sides of this aperture display dissimilar local electrostatic features (Figure 4a,b). With respect to the center of the β cage, half of

the eight SM apertures are directed toward one or another side. The latter feature introduces additional diversity in the EP properties on the overall surface of the cavity.

(52) Murray, L. J.; Dincá, M.; Long, J. R. *Chem. Soc. Rev.* **2009**, *38*, 1294−1314.

(53) Lochan, R. C.; Head-Gordon, M. *Phys. Chem. Chem. Phys.* **2006**, *8*, 1357−1370.

DOI: 10.1021/ic5028256
Inorg. Chem. 2015, 54, 2660−2670